

---

# ECLARE: EFFICIENT CROSS-PLANAR LEARNING FOR ANISOTROPIC RESOLUTION ENHANCEMENT

---

PREPRINT

**Samuel W. Remedios**

Department of Computer Science  
Johns Hopkins University  
samuel.remedios@jhu.edu

**Shuwen Wei**

Department of Electrical and Computer Engineering  
Johns Hopkins University

**Shuo Han**

Department of Electrical and Computer Engineering  
Johns Hopkins University

**Jinwei Zhang**

Department of Electrical and Computer Engineering  
Johns Hopkins University

**Aaron Carass**

Department of Electrical and Computer Engineering  
Johns Hopkins University

**Kurt G. Schilling**

Department of Radiology and Radiological Sciences  
Vanderbilt University Medical Center

**Dzung L. Pham**

Department of Radiology  
Uniformed Services University

**Jerry L. Prince**

Department of Electrical and Computer Engineering  
Johns Hopkins University

**Blake E. Dewey**

Department of Neurology  
Johns Hopkins School of Medicine

March 18, 2025

## ABSTRACT

In clinical imaging, magnetic resonance (MR) image volumes are often acquired as stacks of 2D slices, permitting decreased scan times, improved signal-to-noise ratio, and image contrasts unique to 2D MR pulse sequences. While this is sufficient for clinical evaluation, automated algorithms designed for 3D analysis perform sub-optimally on 2D-acquired scans, especially those with thick slices and gaps between slices. Super-resolution (SR) methods aim to address this problem, but previous methods do not address all of the following: slice profile shape estimation, slice gap, domain shift, and non-integer / arbitrary upsampling factors. In this paper, we propose ECLARE (Efficient Cross-planar Learning for Anisotropic Resolution Enhancement), a self-SR method that addresses each of these factors. ECLARE estimates the slice profile from the 2D-acquired multi-slice MR volume, trains a network to learn the mapping from low-resolution to high-resolution in-plane patches from the same volume, and performs SR with anti-aliasing. We compared ECLARE to cubic B-spline interpolation, SMORE, and other contemporary SR methods. We used realistic and representative simulations so that quantitative performance against a ground truth could be computed, and ECLARE outperformed all other methods in both signal recovery and downstream tasks. On real data for which there is no ground truth, ECLARE demonstrated qualitative superiority over other methods as well. Importantly, as ECLARE does not use external training data it cannot suffer from domain shift between training and testing. Our code is open-source and available at <https://www.github.com/sremedios/eclare>.

## 1 Introduction

Magnetic resonance (MR) imaging (MRI) is an essential clinical tool in diagnosis, monitoring, management and research in many neurological diseases. 2D MR neuroimaging uses slice selection to acquire 2D slices according to a specific slice profile [Brown et al., 2014]. When multiple slices are acquired, these slices are stacked to create a 3D volume. In contrast, 3D MRI uses two phase encode directions to acquire 3D volumes directly [Elmaoğlu and Çelik, 2011]. Although 3D MRI has many advantages, including greater utility in downstream processing, multi-slice 2D MRI still accounts for the majority of clinical scans because it 1) is faster to acquire; 2) offers clinically relevant tissue contrasts difficult to acquire in 3D; 3) has relaxed hardware requirements; 4) is very familiar to clinicians; and 5) is usually less sensitive to motion artifacts. In the national multi-site TREAT-MS pragmatic clinical trial on multiple sclerosis (MS) [Mowry and Newsome, 2024], for example, of 634 baseline scan sessions—all of which were ordered by different MS clinicians to verify MS diagnosis—only 58% of the sessions contain a 3D MR image and 81% of all reviewable scans obtained in these sessions are multi-slice 2D MRI. Multi-slice 2D MRI are also common in pre-clinical imaging studies [Stringer et al., 2021].

Multi-slice 2D MR neuroimages can be strikingly anisotropic. Although in-plane resolutions for 2D MRI are frequently less than 1 mm in both phase-encode and readout directions, slice thicknesses may be 3–8 mm and many acquisitions additionally have slice gaps of 0.5–2 mm. Automated processing pipelines and algorithms, which are often designed and trained for isotropic image volumes, perform sub-optimally on such anisotropic volumes (even when interpolated to have isotropic voxel spacing). Super-resolution (SR) aims to solve this problem by estimating high-resolution (HR) images from low-resolution (LR) acquisitions. Most contemporary work on SR for MRI focuses on deep neural networks. Convolutional neural networks (CNNs) form the backbone of many approaches [Sood and Rusu, 2019, Du et al., 2020], including architectures such as generative adversarial networks (GANs) [Zhang et al., 2022, Chen et al., 2020, Lyu et al., 2020], normalizing flows [Lugmayr et al., 2020, Kim and Son, 2021, Liu et al., 2023, Ko et al., 2023], and denoising diffusion probabilistic models (DDPMs) [Wu et al., 2023, Wang et al., 2023, 2024a, Chang et al., 2024, Han and Huang, 2024, Wu et al., 2024b]. The transformer architecture [Lu et al., 2022, Yang et al., 2020, Yan et al., 2021, Li et al., 2022, Feng et al., 2021] is also common, sometimes used alongside CNNs [Zhou et al., 2023, Forigua et al., 2022, Cheng et al., 2023, Fang et al., 2022].

Although many SR approaches demonstrate remarkable performance, none at present satisfy all desirable properties for SR of multi-slice 2D MRI. Most methods, for example, do not consider the slice profile and true through-plane resolution of 2D MRI. Indeed, many approaches conflate slice separation with through-plane resolution, but they are different concepts and must be handled differently. For example, methods evaluated on simulations that use LR data that is only downsampled from 3D volumes (i.e., with interpolation) and without proper simulation of slice profile and slice separation would be more properly labeled as “inpainting” or “slice imputation” rather than super-resolution. As well, many methods in the literature have been trained for super-resolution of single integer factors such as 2 and 4 [Sood and Rusu, 2019, Zhang et al., 2018, Du et al., 2020, Lugmayr et al., 2020, Wu et al., 2023, Lu et al., 2022, Yang et al., 2020, Zhou et al., 2023]. Not only do these methods need to be retrained for each integer factor that is encountered, they also use techniques like power-of-two upsampling or pixel shuffle [Shi et al., 2016] that do not allow for non-integer factors. Finally, many methods are trained on specific MR tissue contrasts and often (in neuroimaging) on skull-stripped data. Those methods would need to be retrained and possibly re-evaluated for alternative tissue contrasts and for non-skull-stripped data. At present, there is no algorithm that handles all of these concerns for an arbitrary multi-slice 2D MR image volume.

To address these concerns, we propose ECLARE (Efficient Cross-planar Learning for Anisotropic Resolution Enhancement), a deep learning algorithm to super-resolve multi-slice 2D MR volumes along the through-plane direction. ECLARE builds on a succession of self-SR approaches [Jog et al., 2016, Zhao et al., 2018, 2019, 2020, Remedios et al., 2021, 2023], in which all training data is extracted from the LR image volume. However, ECLARE adds several crucial features to properly model slice acquisition, account for non-integer super-resolution factors, and incorporate efficient network design elements. In particular, we use ESPRESO [Han et al., 2021, 2023] to estimate the relative slice selection profile. We use this profile to model slice thickness and gap and to simulate training data from HR in-plane patches extracted from the anisotropic input volume. These data are used to train an efficient SR neural network architecture based on “wide activation SR” (WDSR) [Yu et al., 2018]. The model is then applied to both canonical through-planes, yielding two super-resolved volumes that are then averaged to create the final output. Underlying all interpolation operations in our approach is a novel field-of-view (FOV)-aware interpolation algorithm that respects the FOV center and target sample spacing. The main contributions of this paper are the following:

- We propose an FOV-aware interpolation to resample an image to a new grid while preserving a desired sample spacing and maintaining the location of the FOV.

- We model the relationship between isotropic and anisotropic volumes with explicit slice thickness and slice gap, then leverage ESPRESSO to learn this model.
- We propose an efficient alternative to previous self-SR approaches in MR: a single-model architecture without pre-trained weights to perform both anti-aliasing and SR.
- We propose an architectural change to WDSR to yield the correct number of slices at the correct FOV at both integer and non-integer anisotropy factors.
- We evaluate our approach and compare against several methods in both signal recovery metrics and downstream task performance in two disparate datasets.

The sum of our contributions is a method that super-resolves an anisotropic volume without the need of external training data. This work extends a previously published extension to SMORE [Remedios et al., 2023].

## 2 Related Work

In this work, we consider SR for 2D multi-slice MRI. While there is a body of literature discussing SR approaches focusing on training a model with external data, we do not discuss it here. Such approaches create paired LR-HR data through simulations of large datasets, perform supervised learning with or without consideration of arbitrary scale factors, and either must be applied to a similar domain as the training set or undergo domain adaptation for practical use. Alternatively, in this paper we consider methods that aim to be applicable “out-of-the-box.” Accordingly, our discussion of related work is limited to self-supervised or foundational models for SR of 2D anisotropic MR volumes. Thus, at test-time, the existence of relevant external training data is not assumed.

### 2.1 Self-SR

Self-SR in MRI was first explored [Jog et al., 2016] by fitting an anchored neighborhood regression [Timofte et al., 2013] model to learn the mapping from LR to HR patches, followed by Fourier burst accumulation (FBA) [Delbracio and Sapiro, 2015] to aggregate estimated high frequency Fourier coefficients into the super-resolved volume. The related work SMORE [Zhao et al., 2018, 2020] reinterpreted self-SR using CNNs, which greatly increased the output accuracy and visual appearance. SMORE trains two enhanced deep residual networks (EDSRs) [Lim et al., 2017]: one for anti-aliasing and one for SR. These networks are applied in cascade to orthogonal through-plane slices, and all intermediate results are fused with FBA. Furthermore, although SMORE can be a self-SR method, Zhao et al. [2020] found that pre-training on similar data (i.e., human head MR images) and fine-tuning on the anisotropic volume at test-time allowed fewer training iterations and achieved better results.

### 2.2 INR

Implicit neural representations (INR) [Park et al., 2019, Mildenhall et al., 2020, Sitzmann et al., 2020, Chen et al., 2021, Wu et al., 2022] learn the mapping from coordinate to intensity. Since coordinates can be sampled at any resolution, this has inspired several works related to arbitrary-scale SR [Tan et al., 2020, Zhu et al., 2021, Wu et al., 2022, Liu et al., 2024]. Recently, multi-contrast INR [McGinnis et al., 2023] was proposed to super-resolve subjects with multiple available contrasts from the same session, ideally acquired at different orientations (e.g., sagittal  $T_1$ -w and coronal  $T_2$ -w). However, that method also supports the use of a single contrast, training in a similar manner to self-SR methods. INR approaches cannot directly be used for SR, though. Since they train on bandlimited, sampled data, they cannot be expected to produce reasonable frequencies higher than the training data frequency cutoff, regardless of the queried sampling spacing. Furthermore, often the LR image exhibits blurring and aliasing, so the INR method also must correct for these factors rather than directly estimate the blurred, aliased intensity value.

### 2.3 SynthSR

SynthSR [Iglesias et al., 2023] is a joint synthesis and SR model. Training data for SynthSR includes real MPRAGE head volumes and their corresponding parcellations. Domain randomization uses a Gaussian mixture model to produce synthetic MR-like images of various contrasts that are then augmented with a wide variety of simulated slice thicknesses, slice separations, bias fields, and additive noise. Through domain randomization, SynthSR maps an MR image of arbitrary contrast to a 1 mm isotropic  $T_1$ -w MPRAGE scan.

### 3 Methods

Our proposed method ECLARE improves resolution along the through-plane axis of an anisotropic 2D-acquired multi-slice MR image volume. First, in Sec. 3.1 we model the relationship between HR and LR volumes, which is fully characterized by the slice selection profile and the slice separation. In Sec. 3.2, we describe how we approximate the slice selection profile and the mapping from HR to LR (the “forward model”). Then, in Sec. 3.3, we describe the different choices available for interpolation strategies and propose FOV-aware interpolation. We leverage a method named ESPRESO [Han et al., 2023], which produces a digital estimate of the slice selection profile. We then implement an approximation of our forward model with digital convolutions and our proposed FOV-aware interpolation strategy. In Sec. 3.4, we describe the method to simulate paired LR and HR 2D patches and perform supervised learning to train a 2D deep CNN. In Sec. 3.5, we show how ECLARE uses this 2D CNN to super-resolve the 3D volume along the two canonical through planes. Finally, in Sec. 3.6 we describe implementation details in the final ECLARE algorithm.

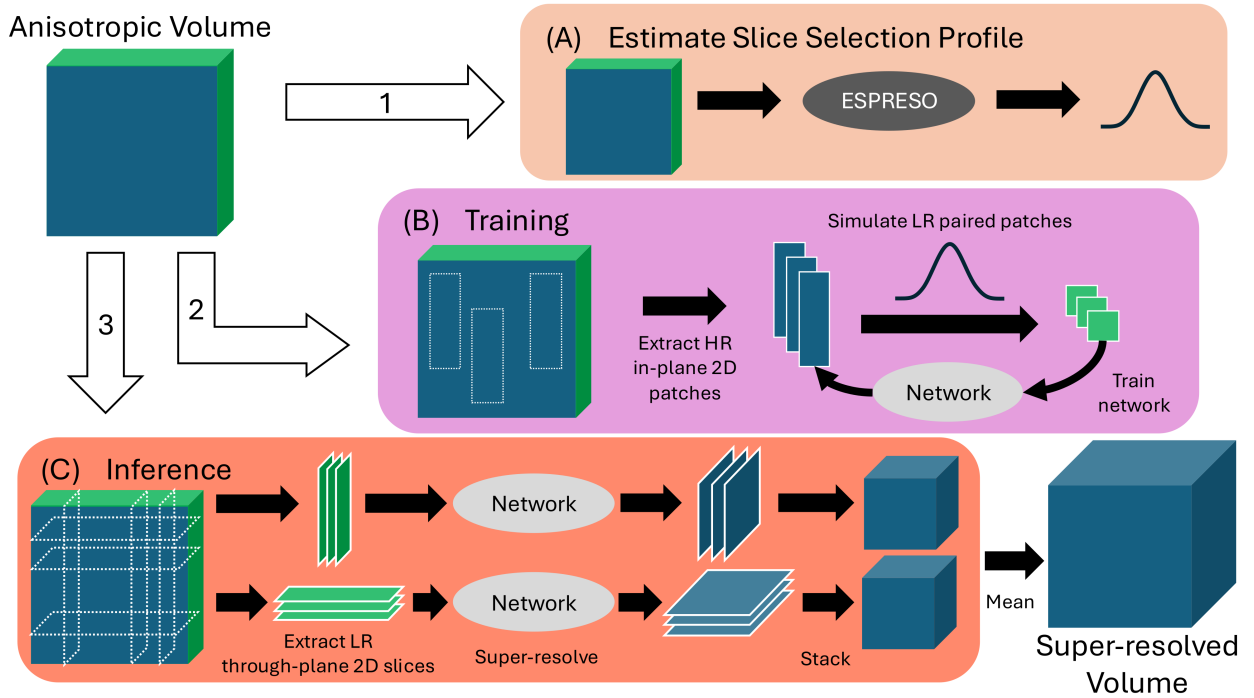


Figure 1: A flowchart of our proposed method. The anisotropic input volume is fed independently into each of the three steps. First, in (A) (Sec. 3.2), we estimate the slice excitation profile with ESPRESO. Second, in (B) (Sec. 3.4), we extract HR in-plane 2D patches and use the PSF estimated from (A) to create paired training data. This training data is used to train the network with supervised learning. Third, in (C) (Sec. 3.5), we extract LR through-plane 2D slices and super-resolve them with the trained network from (B). The super-resolved slices are stacked and averaged, yielding the super-resolved output volume.

#### 3.1 Modeling the imaging process

A 2D-acquired MR image volume is a stack of independent 2D slices. In-plane, data is acquired in k-space and transformed to the image domain through the inverse Fourier transform. For through-plane, the relationship between slices is entirely characterized in the image domain. Along the through-plane axis, a magnetic gradient causes atomic nuclei to resonate at different frequencies. This means that resonant frequencies along this axis correspond to different spatial locations. Slice selection is a bandpass filter that selects frequencies (again, corresponding to spatial location) that are to be excited. The *slice selection profile*, (equivalently, “slice profile”) is the shape of the bandpass filter. Although the ideal form of the slice selection profile is a rect function, which would excite only the through-plane positions corresponding to the slice of interest and nothing else, in practice this is unachievable. Instead, common slice profiles take the shape of truncated Gaussians or use the Shinnar-Le Roux algorithm [Pauly et al., 1991, Shinnar et al., 1989] to approximate a rect. Assuming homogeneity in the imaging process, within its frequency band the slice

selection profile excites all atomic nuclei equally. This means all in-plane measurements are subject to the same slice thickness and location.

We denote the slice selection profile as  $h$ . It is a continuous function of the through-plane position. We note that although slice selection is implemented as a bandpass filter, relative to a particular through-plane axis position the slice profile is a low-pass filter. This corresponds to the observation that ideal slice profiles are rect-like or Gaussian-like.

The desired image volume  $x$  is HR and isotropic with resolution  $a \times a \times a$  mm. In this work we consider it to also be a 2D-acquired multi-slice MR volume with slice thickness equal to the slice separation (i.e., no gap). In reality, acquiring such image volumes is not practical; 3D acquisitions are preferred. However, for simplification we consider only 2D-acquisitions. Now, the observed image volume  $y$  is LR and anisotropic. Its resolution  $a \times a \times b$  mm is the same as the HR volume in-plane but worse along the through-plane axis:  $b > a$ . Additionally,  $y$  may have slice gap, so the slice separation may be greater than the slice thickness. We model 2D multi-slice acquisitions as a discrete convolution between the unobserved HR image volume and the slice selection profile:

$$y = (x * h) \downarrow_r, \quad (1)$$

where  $\downarrow_r$  is the subsampling ratio of  $r$ . The full-width-at-half-max (FWHM) of  $h$  determines the slice thickness (alongside the HR slice thickness  $a$ ) and  $r$  is a ratio between the HR slice separation  $s^*$  and the LR slice separation  $s$ . We define this factor as  $r = \frac{s}{s^*}$ . If  $h$  has a smaller FWHM than the separation  $s$ , then Eq. 1 models slice gap. Similarly, a FWHM of  $h$  equal to or greater than  $s$  respectively models adjacent slices and slice overlap.

### 3.2 Approximating the imaging process

The imaging process described with Eq. 1 comprises blurring with  $h$  and subsampling by  $r$ . In this subsection we discuss how we approximate both of these. In general, the slice selection profile  $h$  is proprietary to the scanner manufacturer and cannot be derived precisely. We leverage ESPRESO [Han et al., 2023] to estimate  $h$ , shown in Fig. 1 (A). Briefly, ESPRESO optimizes a neural network to produce a fixed-size discrete  $h$  by adversarial training. It trains on a single LR anisotropic volume by assuming that degraded in-plane patches and through-plane patches are indistinguishable from one another for an appropriate patch size. That is, ESPRESO assumes in-plane and through-plane patches come from the same distribution. Thus, in-plane image patches are extracted, degraded by  $h$ , and judged through a discriminator against through-plane patches. An optimal  $h$  yields degraded in-plane image patches that are indistinguishable from true through-plane image patches. Every component is now present for Eq. 1:  $h$  is approximated by ESPRESO and  $r$  is known since we have a HR slice separation and LR slice separation.

### 3.3 FOV-aware interpolation

While interpolation is a routine operation in digital signal processing, the exact implementation in software has several freedoms. ECLARE requires both downsampling (for training data simulation) and upsampling (for inference) and we would like both to be stable with respect to the FOV. We consider three conditions that are desirable to meet with respect to the FOV of the signal:

1. the center of the FOV should be at the same location;
2. the samples should be spaced as specified;
3. the extents of the FOV should be maintained.

Interpolation algorithms cannot meet all of these conditions in general since only a discrete number of samples is permitted. However, since it is possible to satisfy two of these conditions, a compromise on the third is necessary. We quickly review popular modern implementations. The implementation `scipy.ndimage.zoom` [Virtanen et al., 2020] meets conditions 1) and 3). It adjusts the sample spacing to preserve the FOV center and extents. The implementation `torch.nn.functional.interpolate` [Paszke et al., 2019] meets only condition 2). It preserves the sample spacing, but neither the FOV center nor the extents. Instead, it anchors the beginning of the FOV to match the input. In our work, we place more importance on the center of the FOV and the sample spacing and therefore desire conditions 1) and 2). We summarize the interpolation method proposed in [Han, 2022] that maintains the FOV center and sample spacing while sacrificing the extents of the FOV. A comparison of the three implementations is shown in Fig. 2.

As in Han [2022], we introduce a fixed coordinate system for the signal before and after interpolation. Let the position of the first pixel be centered at zero, let  $N$  be the number of pixels before interpolation, and let the spacing before interpolation be one. The width of each pixel equals the spacing; before interpolation it is therefore also one. The first pixel  $p_0$  is centered at zero and the last pixel  $p_{N-1}$  is centered at  $N - 1$ . Since each pixel has a width of one,  $p_0$  extends from  $-0.5$  to  $0.5$  and  $p_{N-1}$  extends from  $N - 1.5$  to  $N - 0.5$ . Therefore the entire image extends from  $-0.5$  to  $N - 0.5$ .

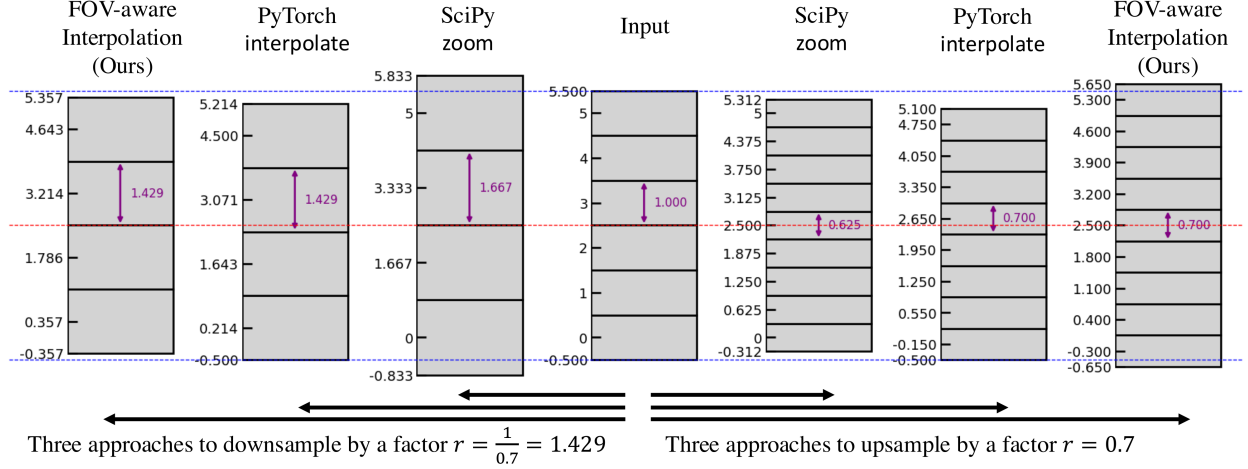


Figure 2: A 1D demonstration of the differences between interpolation implementations. The input has 6 pixels and its FOV center is located at 2.5, indicated by the red dashed line. Its sample spacing is 1, indicated by the purple arrow. Its extents occur at -0.5 and 5.5, indicated by the blue dashed line. In this demonstration, the desired sample spacing for upsampling is 0.7, and the desired sample spacing for downsampling is 1.429. The implementation `scipy.zoom` [Virtanen et al., 2020] maintains the FOV center, but changes the sample spacing to 0.625 and 1.667 for upsampling and downsampling, respectively. The implementation `torch.nn.functional.interpolate` [Paszke et al., 2019] anchors the FOV extent to start at 0.5, shifting the center from the desired FOV center. Our proposed method (Sec. 3.3) maintains both the sample spacing and the FOV center.

We now calculate the new positions and extents of pixels after interpolation with respect to the same coordinate system. Let the new spacing (and pixel width) be  $d$ . After interpolation, the new image must have an integer number of pixels. With  $N'$  as the number of pixels after interpolation and  $\lfloor \cdot \rfloor$  as the rounding operator,

$$N' = \left\lfloor \frac{N}{d} \right\rfloor. \quad (2)$$

This allows us to notate the first pixel after interpolation as  $p'_0$  and the last pixel as  $p'_{N'-1}$ .

In order to center around the same FOV, the center position of the entire image should be identical before and after interpolation. Since the center of the FOV is the halfway point between the first and last pixels, we can write

$$c = \frac{1}{2}(p_0 + p_{N-1}) = \frac{1}{2}(p'_0 + p'_{N'-1}) \quad (3)$$

Also, since we know the new spacing  $d$  and the new number of pixels  $N'$ , we can calculate the position of any pixel  $p_i$ ,  $i = 0, 1, 2, \dots, N' - 1$  in terms of the new starting pixel:

$$p'_i = p'_0 + di. \quad (4)$$

To find the position of the first pixel  $p'_0$ , we use the center  $c$ :

$$c = \frac{1}{2}(p'_0 + p'_{N'-1}) \quad (5)$$

$$= \frac{1}{2}(p'_0 + [p'_0 + d(N' - 1)]) \quad (6)$$

$$p'_0 = -\frac{d}{2}(N' - 1) + c. \quad (7)$$

Finally, we can calculate the extents of the entire image after interpolation. The first pixel extends from  $p'_0 - \frac{d}{2}$  to  $p'_0 + \frac{d}{2}$  and the last pixel extends from  $p'_{N'-1} - \frac{d}{2}$  to  $p'_{N'-1} + \frac{d}{2}$ . Thus, the image extents are  $p'_0 - \frac{d}{2}$  to  $p'_{N'-1} + \frac{d}{2}$ .

The result of this method yields an FOV-aware interpolation implementation that maintains the FOV center and guarantees the desired pixel spacing. This is true in both upsampling and downsampling scenarios and is demonstrated in Fig. 2.

### 3.4 Training a deep learning model with paired data

We now develop a relationship between in-plane and through-plane data and train a SR network. The supervised learning framework in SR requires paired LR and HR data. We extract HR 2D patches from in-plane and produce blurred 2D patches using Eq. 1 with the learned  $h$  from ESPRESO. These blurred 2D patches are then downsampled using the FOV-aware interpolation described in Sec. 3.3. Thus, each LR patch has the appropriate simulated slice thickness and separation while additionally being FOV-centered according to the HR patch.

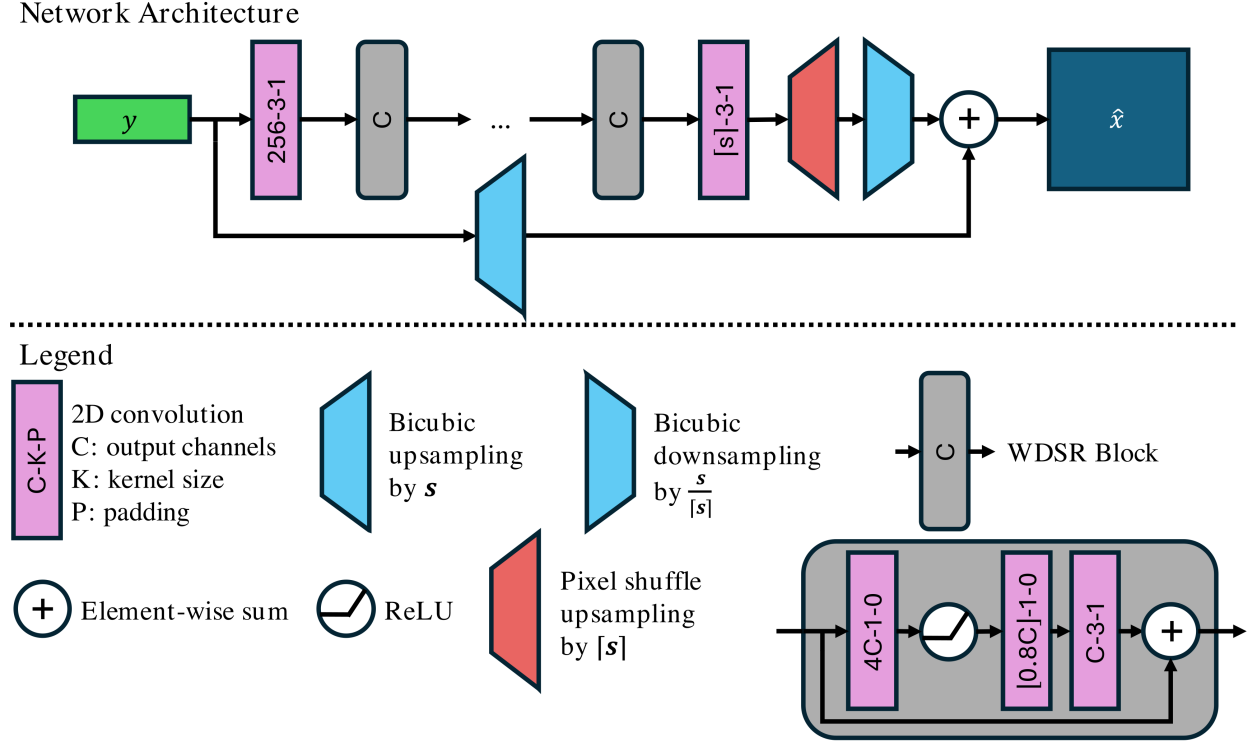


Figure 3: A diagram of our proposed architecture, based on WDSR [Yu et al., 2018]. The low resolution image  $y$  is first processed by a convolution to produce a feature map with 256 channels. Simultaneously, it is upsampled to produce an interpolated image to be used later as a skip connection. It then passes through several WDSR blocks. A final convolution is done to produce the correct number of channels for pixel shuffle. Finally, the result is downsampled and added to the skip connection to yield the output. In our implementation, we set  $C$  to 256 and use 16 WDSR blocks.

A deep convolutional neural network model learns the mapping between the paired patches, as shown in Fig. 1 (B). We use an architecture based on WDSR [Yu et al., 2018] after empirically evaluating other architectures such as EDSR [Lim et al., 2017] and RCAN [Zhang et al., 2018]. The WDSR architecture, designed for efficiency, achieved the same quantitative metrics as other architectures but trained in less time. However, the WDSR architecture itself uses pixel shuffle [Shi et al., 2016], which requires integer upsampling factors, to perform the final upsampling to the desired image size. In general, though,  $r$  may be non-integer. To address this, we rewrite  $r$  as

$$r = \lceil r \rceil \frac{r}{\lceil r \rceil}, \quad (8)$$

where  $\lceil \cdot \rceil$  is the ceiling operation. We therefore first pixel shuffle to overshoot the target image size and downsample to reach the target image size. The downsampling is performed using the interpolation method described in Sec. 3.3. Our model is illustrated in Fig. 3.

### 3.5 Inference

The trained network is fully convolutional, allowing it to be used on full-sized image slices despite training on patches. Our inference strategy to super-resolve the volume is to independently super-resolve all slices from each canonical

through-plane axis, stack the super-resolved slices into two volumes, and take an unweighted mean of the two volumes to produce the final output. This procedure is illustrated in Fig. 1 (C).

### 3.6 Implementation details

ECLARE is implemented in PyTorch and we train the model from scratch with each new multi-slice 2D MR image. We optimize the parameters of the network by minimizing mean squared error using a total of 1,000,000 patches with a batch size of 128 patches. The training patches are of size  $\lceil 8r \rceil \times 8$ . We use a 21-tap filter to represent  $h$ , which follows the standard implementation of ESPRESO. We used the Adam [Kingma and Ba, 2014] optimizer, a learning rate of  $10^{-3}$ , the one-cycle learning rate scheduler [Smith and Topin, 2019], and PyTorch’s automatic mixed precision feature. Our implementation uses 16 residual blocks of 256 channels. With these hyperparameter choices, on an NVIDIA V100 the total running time, including self-training and inference, is just under 5 minutes. The memory usage is 1.16 GB on the GPU. Our code is open-source and is available at <https://www.github.com/sremedios/eclare>.

## 4 Experiments and Results

To determine the efficacy of ECLARE, we designed two simulation experiments and one experiment for real-world evaluation.

### 4.1 Data and evaluation metrics

The simulation experiments began with HR isotropic 3D-acquired image volumes of resolution  $1 \times 1 \times 1 \text{ mm}^3$ . These images were then degraded with Eq. 1, setting  $h$  to the shape of the slice excitation profile created by the Shinnar-Le Roux (SLR) pulse design algorithm [Pauly et al., 1991, Shinnar et al., 1989],  $s$  to the desired slice spacing (described below), and  $x$  to a 3D-acquired isotropic volume. The implementation of the SLR algorithm we use is from the `sigpy` library [Martin et al., 2020].

The physical dimensions of the slice thickness is determined by the FWHM of the slice selection profile. Since our images began with 1 mm thick slices, this involved choosing the FWHM of  $h$  to be equal to the desired slice thickness. In clinical neuroimaging, it is common to acquire no slice gap or a slice gap equal to 1 mm or  $1/3$  the slice thickness, so we chose to simulate 2D acquisitions of thicknesses 3, 4, and 5 mm with gaps 0, 1, 1.2, and 1.5 mm, yielding a total of 8 resolutions. We adopt the notation  $T\|G$  [Remedios et al., 2023] for a thickness of  $T$  mm and gap of  $G$  mm and list our choices here: (3||0), (3||1), (4||0), (4||1), (4||1.2), (5||0), (5||1), and (5||1.5). These simulation experiments were conducted on two datasets. The first consisted of 50  $T_1$ -weighted ( $T_1$ -w) images from healthy subjects in OASIS-3 [LaMontagne et al., 2019]. The second consisted of 30  $T_2$ -weighted ( $T_2$ -w) FLuid Attenuated Inversion Recovery (FLAIR) images from people with MS in 3D-MR-MS dataset [Lesjak et al., 2018].

We compare ECLARE to bicubic interpolation, SynthSR [Iglesias et al., 2023] (Sec. 2.3), single-contrast INR [McGinnis et al., 2023] (Sec. 2.2), and SMORE [Zhao et al., 2020]. Since its output is always a  $T_1$ -w MPRAGE, we do not evaluate SynthSR on the FLAIR SR task.

To highlight the advantages of the independence from external training data, we also show results on a variety of real-world data, as follows,

1. a 5||1  $T_2$ -w FLAIR scan of a human head from the ultra low-field (ULF) (0.3T) M4Raw dataset [Lyu et al., 2023] with an SR factor of  $r = 6$ ;
2. a 3||0 susceptibility-weighted image (SWI) of a human brain with an in-plane resolution of  $0.4 \times 0.4 \text{ mm}$  at 7T from an in-house dataset at Vanderbilt, with an SR factor of  $r = 7.5$ ;
3. a 0.4||0  $T_2$ -w scan of a mouse head with an in-plane resolution of  $0.1 \times 0.1 \text{ mm}$  on a 7T scanner from an in-house dataset from Uniformed Services University [Guo et al., 2024], with an SR factor of  $r = 4$ ; and
4. a 6||0 with an in-plane resolution of  $0.6 \times 0.6 \text{ mm}$   $T_2$ -w scan of a human spine on a 3T scanner from an in-house dataset from Vanderbilt, with an SR factor of  $r = 10$ .

For these real-world data, as no ground truth images are available, results are purely qualitative. Additionally, since none of the images are  $T_1$ -w MPRAGE human heads, SynthSR was excluded from this evaluation; thus the comparison methods included bicubic interpolation, single-contrast INR, SMORE, and ECLARE.

Since we have ground truth (GT) images for simulated data, we can use reference-based image quality metrics to evaluate SR performance. We use peak signal-to-noise ratio (PSNR) and structural similarity index measure (SSIM) with the implementations provided by the `scikit-image` Python library [Van der Walt et al., 2014]. We additionally

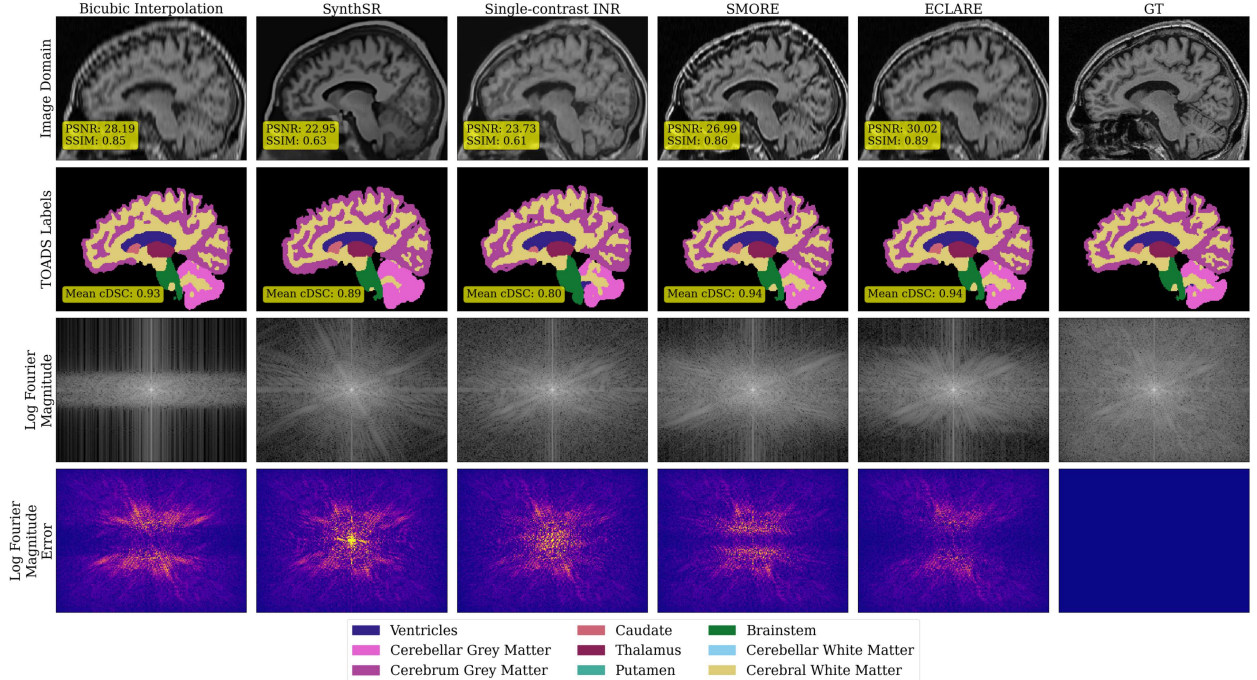


Figure 4: A  $5\|1.5$  sagittal slice from a representative subject from the OASIS-3 dataset. The first row shows the image domain with PSNR and SSIM for the entire image volume overlaid. The second row shows the simplified SLANT labels, with an overlay showing the mean cDSC across all labels for the entire image volume. The third row shows the log Fourier magnitude of the corresponding slice. The fourth row shows the absolute difference between the log Fourier magnitudes of the SR method and the ground truth.

evaluate the utility of the super-resolved images by segmentation downstream tasks. We use the *consistency Dice similarity coefficient* (cDSC), which we define as the Dice similarity coefficient (DSC) between an automated algorithm’s performance on the HR image volume and the super-resolved image volume. This is to differentiate cDSC from DSC which commonly is used between an algorithm-generated label and a human-generated label.

## 4.2 Healthy $T_1$ -w simulations

We calculated cDSC on the SLANT [Huo et al., 2019] and SynthSeg [Billot et al., 2023] estimates of the OASIS-3 dataset. Since SLANT produces many small labels, we simplify them down to 9 labels as in our previous work [Remedios et al., 2023]: ventricles, cerebellar gray matter (GM), cerebellar white matter (WM), cerebral GM, cerebral WM, caudate, putamen, thalamus, and brainstem. SynthSeg is a generalized automated segmentation technique designed to be robust to a variety of image appearances. It directly produces volume estimates of similar regions of interest, so we include the following comparable regions: ventricles, cerebral white matter, cerebral gray matter, cerebellar white matter, cerebellar gray matter, thalamus, putamen, caudate, and brainstem.

On the OASIS-3 dataset, we show qualitative results from a representative subject at  $5\|1.5$  resolution in Fig. 4. The image domain is shown alongside the SLANT result labels, the log Fourier magnitude, and the error in log Fourier magnitude across the methods. In the image domain, it is apparent that our proposed ECLARE method is visually closer to the ground truth (GT) in both appearance and contrast. Viewing Fig. 4 column-by-column, in the image domain bicubic interpolation does not address the extreme aliasing, but is relatively accurate with respect to the SLANT labels. In the Fourier domain, bicubic interpolation does not recover high-frequency information, and thus the error shown in the Fourier magnitude is only in high-frequency areas. SynthSR generates realistic brain and head appearance, but mismatches the contrast and hallucinates some structures such as the cortical sulci that can be seen in the SLANT labels row. Since SynthSR regenerates the entire image, we see a loss of resolution in the Fourier domain along the anterior-posterior axis as well as yielding an error at zero frequency (i.e., a change in DC). Single-contrast INR does not generate accurate results in the image domain, and actually synthesizes a different brain stem appearance from the other methods, as shown in the green brainstem label in the second row. However, single-contrast INR does generate

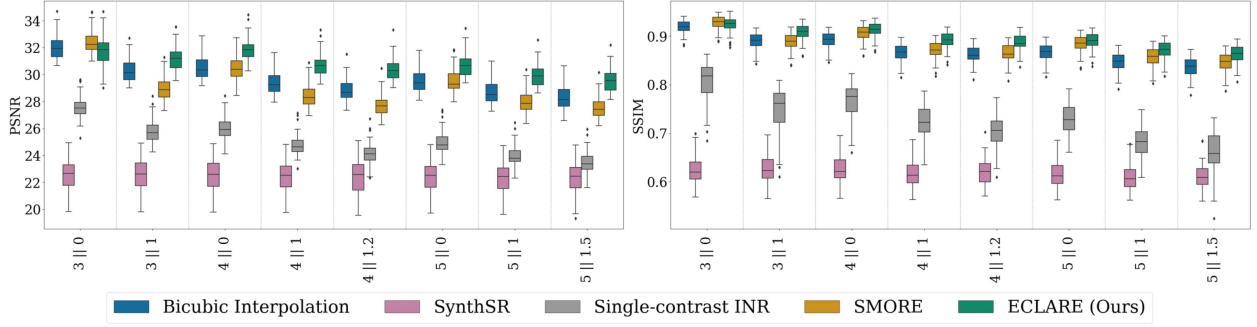


Figure 5: Quantitative results (PSNR on the left, SSIM on the right) on the OASIS-3 dataset across resolutions.

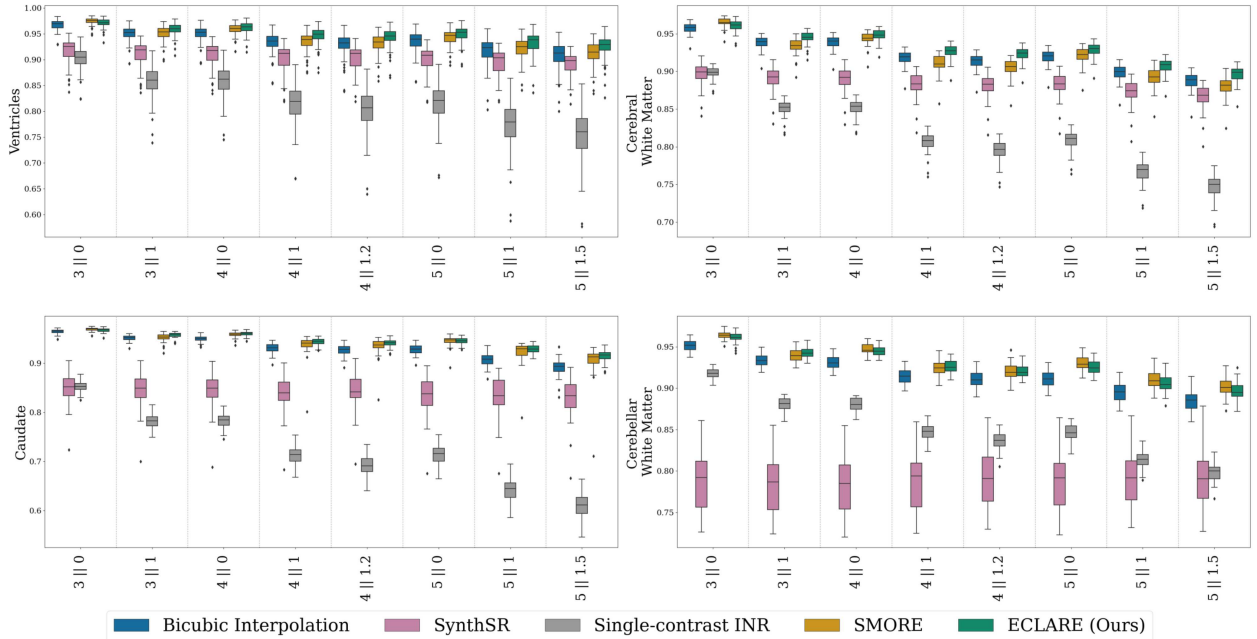


Figure 6: Quantitative results on cDSC by anatomical region on the OASIS3 dataset across resolutions. In the interest of space, only four representative regions (namely, ventricles, cerebral white matter, caudate, and cerebellar white matter) are shown.

the most high-frequency components in Fourier space, though it also makes errors in low-frequency regions. The image domain results for SMORE highlight an “over-sharpening” effect with hyperintense regions near the skull and superior to the ventricles and the bottom part of the brainstem. As shown in the log Fourier magnitude error row of Fig. 4, both SMORE and ECLARE makes fewer errors in the low-frequency regions of Fourier space. However, our proposed ECLARE improves upon the results of SMORE, yielding the most visually accurate image of the group and the least low-frequency errors in Fourier space, even compared to bicubic interpolation. The SLANT segmentation results are still not ideal for any method, and some areas of cortical gray matter are missed by all methods.

We show the PSNR and SSIM for the five methods in Fig. 5. Across all resolutions, our proposed ECLARE outperforms all other methods in both metrics except for the resolution 3||0, where SMORE is best. SMORE’s superiority at 3||0 is likely due to two reasons: 1) SMORE does not have a model of slice gap, and therefore will have peak performance when no gap is present in the data; and 2) SMORE relies on pre-trained weights and was primarily tested and evaluated at data of resolutions 2||0 and 3||0.

In Fig. 6, we show the cDSC for the nine regions of interest calculated by SLANT [Huo et al., 2019]. Overall we see similar trends as in Fig. 5, with ECLARE performing best at all resolutions except at 3||0, where SMORE performs

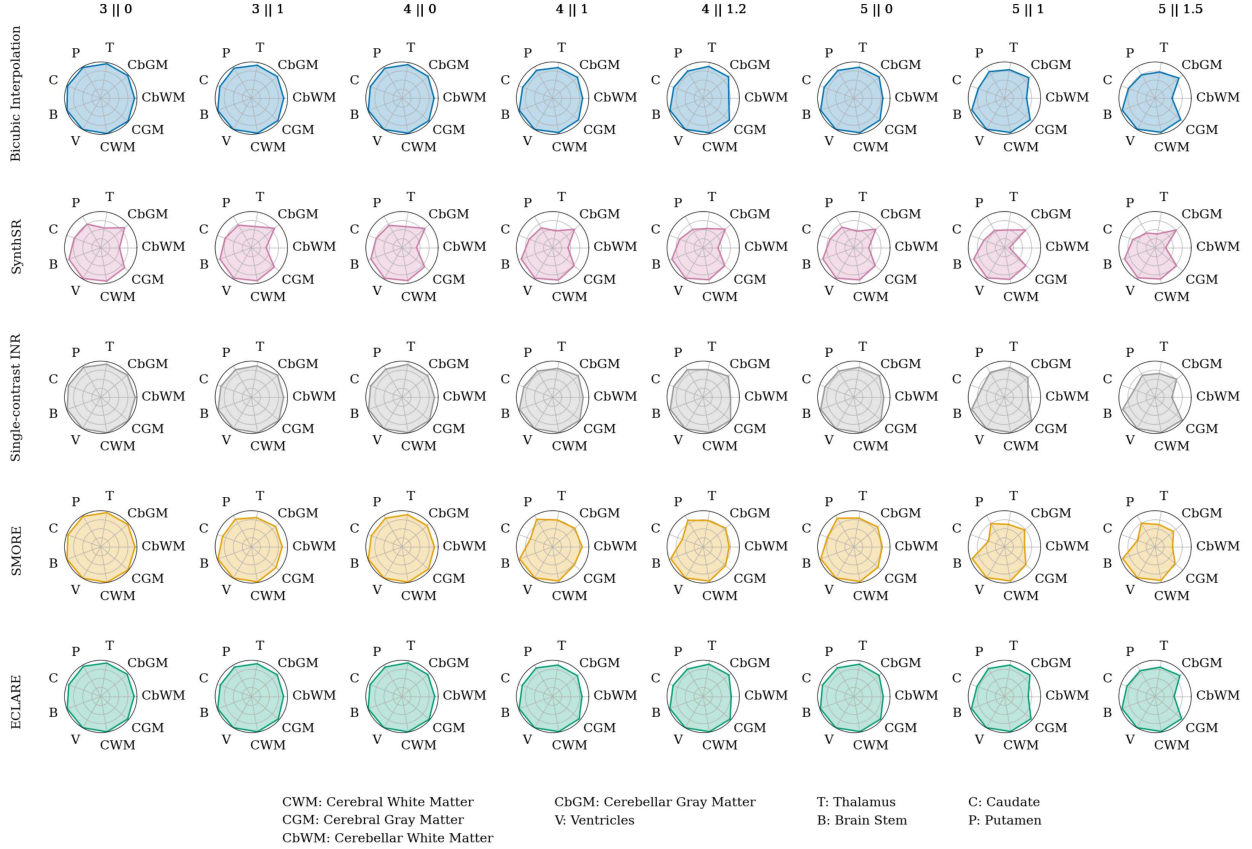


Figure 7: Radar plots showing the  $R^2$ -value for a linear regression of all  $N = 50$  subjects between SynthSeg volume estimation on the super-resolution method vs. the SynthSeg volume estimation of the ground truth.

best. An exception to this is the cerebellar white matter, where at nearly every resolution SMORE is most performant. An interesting observation is how robust SLANT is to interpolation artifacts; bicubic interpolation outperforms the other two super-resolution methods consistently across all resolutions and structures.

We also used SynthSeg [Billot et al., 2023] as a downstream task. For all subjects, we fit a linear regression model to the sets of estimated volumes against the GT volumes per region per resolution where the dependent variable was the GT volume and the independent variable was the SR volume. The fit of the line is quantified by the  $R^2$  coefficient of determination, which we plot in Fig. 7. Some regions (ventricles, cerebral white matter, brainstem) are consistently well-segmented at all resolutions across all SR methods, but others show clear winners. ECLARE outperforms all methods consistently, visualized by the enclosure of other methods on the radar plots.

### 4.3 People with MS: $T_2$ -w FLAIR simulations

For the 3D-MR-MS dataset, we used the automated white matter lesion segmentation algorithm SELF [Zhang et al., 2024] to produce labels for the GT and super-resolved volumes, comparing results with cDSC. We also included signal recovery metrics PSNR and SSIM as with the previous dataset.

We performed similar analyses for the 3D-MR-MS dataset, but with SynthSR omitted due to the image being  $T_2$ -w FLAIR. Qualitative results are shown in Fig. 8, where the first row in the image domain overlays the automated segmentation by SELF in neon-green. This  $T_2$ -w FLAIR is a prime example of the “over-sharpening” artifact from SMORE, such as the hyperintense region just inferior to the ventricle. Many such examples of hyperintense regions just inferior to a dark surface are visible in this result, whereas ECLARE does not exhibit this. Furthermore, ECLARE better recovers from aliasing artifacts induced by the gap, since this image is  $4||1.2$ . Again, from the third row, it is apparent that single-contrast INR changes DC.

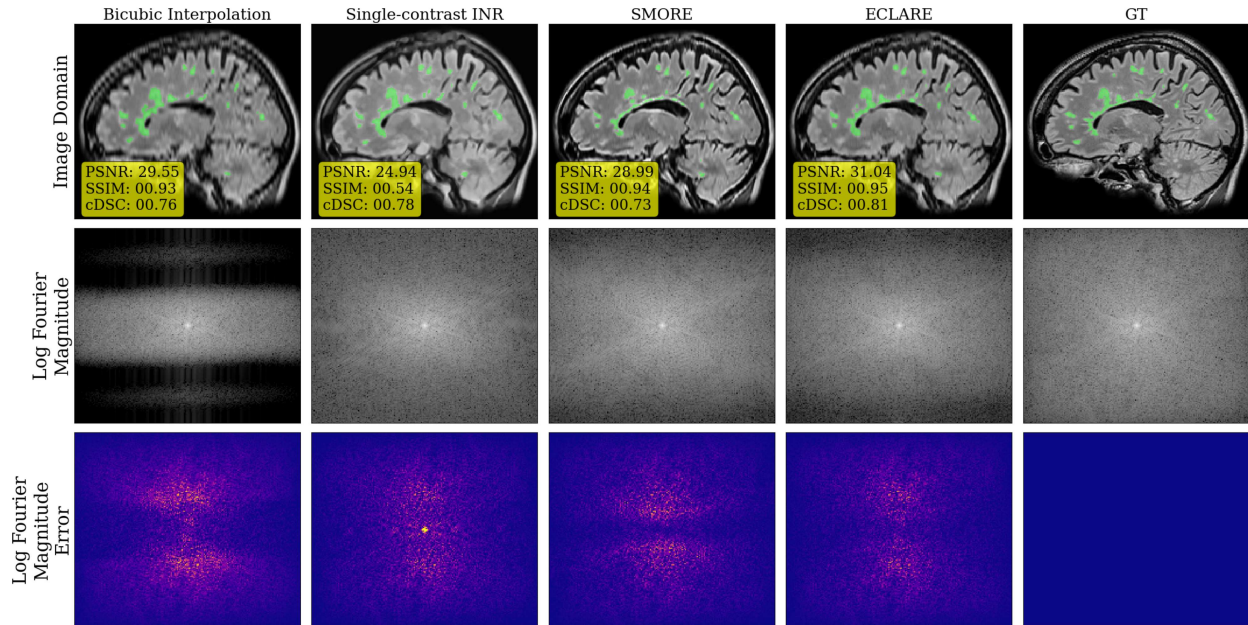


Figure 8: A  $4 \parallel 1.2$  mid-sagittal slice for a representative subject from the 3D-MR-MS dataset. The first row shows the image domain with the automated lesion segmentation overlaid in neon-green. The second row shows the log Fourier magnitude of the corresponding slice. The third row shows the absolute difference between the log Fourier magnitudes of the SR method and the ground truth. The PSNR, SSIM, and cDSC for the entire image volume of this representative are overlaid in the image domains.

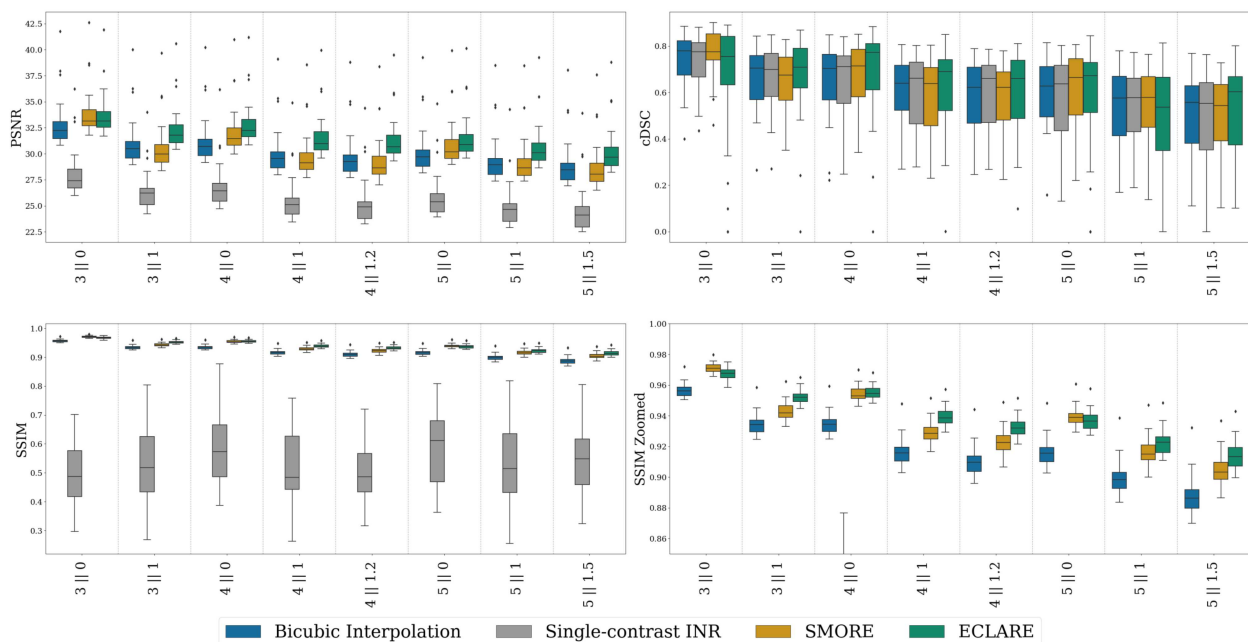


Figure 9: Quantitative results (PSNR in the top-left, cDSC in the top-right, SSIM in the bottom-left, and a zoomed y-axis of SSIM in the bottom-right) on the 3D-MR-MS dataset across resolutions. The bottom-right zoomed SSIM is to better illustrate comparisons between methods with more accurate SSIM scores.

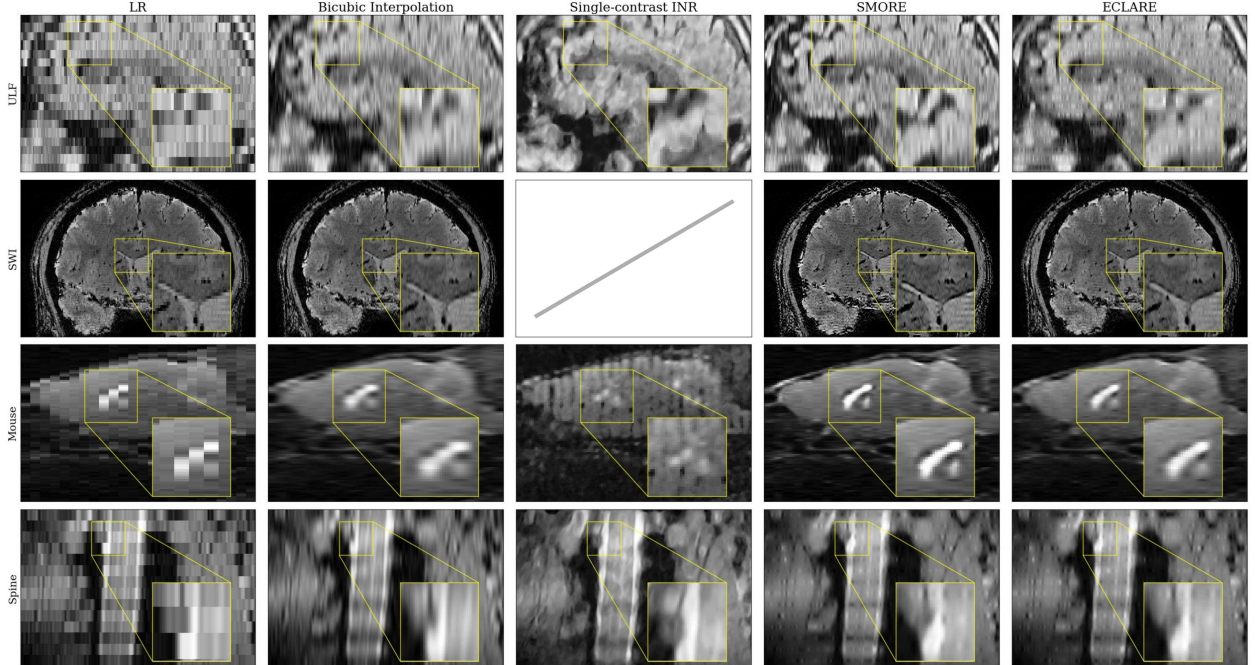


Figure 10: Results on real data for which there is no ground truth. The first column shows the nearest-neighbor interpolated LR data and the second column shows the cubic B-spline interpolated result. The third column shows Single-contrast INR, the fourth column shows SMORE, and the final column shows ECLARE. The first row is the ULF scan, the second is SWI, the third is the mouse scan, and the fourth is the spine.

In Fig. 9, we show the PSNR and SSIM for signal recovery and cDSC for lesion segmentation consistency. Like in the OASIS-3 dataset results, SMORE is the only competitor quantitatively at  $3||0$ , though in this case it is not a clear winner. The upper quartile appears to outperform ECLARE, but the mean is lower. These results are consistent across all three metrics. After  $3||0$ , ECLARE outperforms the rest.

#### 4.4 Real-world data

We evaluated ECLARE alongside bicubic interpolation, single-contrast INR, and SMORE for the SR of real-world data described in Sec. 4.

The results of each of these are shown in Fig. 10, with the nearest neighbor interpolation shown as LR, and each method in subsequent columns. We make two quick notes about single-contrast INR here. First, single-contrast INR was unable to process the SWI image because of its memory requirements, so its result is omitted from the figure. Second, single-contrast INR does not include a model of slice thickness in its formulation; the PSF is assumed to be Dirac. This makes single-contrast INR more of an “inpainting” technique during training rather than super-resolution, since at inference-time the blurred signal will not be deblurred, which is detrimental to the results of single-contrast INR.

The advantage of SMORE and ECLARE is apparent by inspection: aliasing is reduced and images have less blurring than bicubic interpolation. This is evident throughout the representative slices on the ULF, Mouse, and Spine images. The zoomed inset for all images is also illustrative of differences between the proposed methods. For the ULF scan, single-contrast INR is unable to estimate an image that is as realistic as both SMORE and ECLARE.

On the ULF and spine images, we notice both SMORE and ECLARE exhibit a kind of periodic banding spanning the image from left to right. On close examination, this band is approximately equivalent to the interpolated signal at that location. We hypothesize that at large  $r$  values, it is difficult for either method to fill in the unknown information. However, both SMORE and ECLARE are able to respect the original signal at those locations (likely due to how they were trained) and thus the banding appears. Solving this issue is left to future work.

## 5 Discussion and conclusions

In this work, we presented ECLARE as a novel self-SR algorithm for anisotropic volumes that requires no external training data. We presented a model of the imaging process in 2D multi-slice MRI and used ESPRESO to estimate the slice selection profile. With an estimated slice profile, slice thickness and slice separation are both modeled, allowing for training data simulation from the HR in-plane data already present in the anisotropic volume. ECLARE uses a neural network architecture based on WDSR to efficiently train weights from scratch in a short amount of time, taking approximately 5 minutes on a single NVIDIA V100 GPU with a memory footprint under 2 GB. The result is a SR technique that respects the LR image contrast and pathology presence, does not require external training data, and produces HR image volumes with the correct digital resolution in a reasonable amount of time. When compared to four other approaches on two simulated datasets, our approach achieved superior quantitative and qualitative results with respect to signal recovery metrics PSNR and SSIM as well as a downstream task metric—cDSC for brain region and MS lesion segmentation. When looking at results for real-world data, qualitative differences show the utility of ECLARE.

We note two primary limitations of our work here. First, the results from ECLARE do not appear to recover the full isotropic spatial resolution compared to the ground truth images. As apparent from Figs. 4 and 8, high frequency information (details) are absent from the predicted result. The reason for this is two-fold. First, our optimization objective function is solely mean squared error, which is known to lead to blurrier results when used in SR tasks. We also optimized L1, but found nearly identical results qualitatively and quantitatively. Methods that model a distribution, such as adversarial approaches or denoising diffusion probabilistic models, yield improved realism and may lead to improvements in ECLARE. However, the perception-distortion tradeoff [Blau and Michaeli, 2018] asks us to choose between realistic appearances and signal recovery, and we chose the latter. Additionally, modeling distributions potentially introduces the risk of domain dependence. Second, because ECLARE is a self-SR method the in-plane data used as HR reference is not truly HR; it is subject to partial volume effects due to through-plane blurring. This affects ECLARE twice: 1) the target HR data is not representative of true HR slices, and 2) if ESPRESO is used to estimate  $h$  but the volume is highly anisotropic, the resulting kernel may be a spike. These issues may be amended by including a reference HR image volume as a single example to learn from.

The SR of medical images has been a research area for decades. Data-driven approaches now dominate the field of SR, yet the problem is far from solved. When the test-time image does not belong to the training domain, performance of trained approaches is undefined. In medical imaging, domain issues may occur across a number of axes, including resolution difference, anatomical variance, presence of pathology, differences in contrast or scan acquisition parameters, noise level and distribution mismatch, or others. When the test-time image does belong to the training domain, it is unknown whether the super-resolved image is reliable for downstream analysis. Further work is needed to investigate the extent to which an SR algorithm is reliable. Analysis is also needed to determine what slice thicknesses, separations, and profile shapes are best suited for SR and reliability. As these problems are addressed in the future, both the field of SR and the ability of SR to make meaningful clinical impact and research impact will advance forward.

### Disclosures

This research is based on technology described in U.S. Patent No. 12, 067, 698, titled "*Machine learning processing of contiguous slice image data*," assigned to Jerry L. Prince, Can Zhao, and Aaron Carass.

### Acknowledgments

This material is supported by the National Science Foundation Graduate Research Fellowship under Grant No. DGE-1746891 (Remedios). Development is partially supported by NIH ORIP grant R21 OD030163 (Pham). This work also received support from National Multiple Sclerosis Society RG-1907-34570 (Pham), FG-2008-36966 (Dewey), CDMRP W81XWH2010912 (Prince), NIH K01EB032898 (Schilling), and the Department of Defense in the Center for Neuroscience and Regenerative Medicine. The opinions and assertions expressed herein are those of the authors and do not reflect the official policy or position of the Uniformed Services University of the Health Sciences or the Department of Defense.

### References

- Robert W Brown, Y-C Norman Cheng, E Mark Haacke, Michael R Thompson, and Ramesh Venkatesan. *Magnetic resonance imaging: physical principles and sequence design*. John Wiley & Sons, Ltd, 2014.
- Muhammed Elmaoğlu and Azim Çelik. *MRI handbook: MR physics, patient positioning, and protocols*. Springer Science & Business Media, 2011.

- Ellen M. Mowry and Scott D. Newsome. TREAT-MS: Trial of Early Aggressive versus Escalation Therapy in Multiple Sclerosis. <https://treat-mstrial.org/>, 2024. ClinicalTrials.gov Identifier: NCT03500328, Accessed: 2024-06-17.
- Michael S Stringer, Hedok Lee, Mikko T Huuskonen, Bradley J MacIntosh, Rosalind Brown, Axel Montagne, Sarah Atwi, Joel Ramirez, Maurits A Jansen, Ian Marshall, et al. A review of translational magnetic resonance imaging in human and rodent experimental models of small vessel disease. *Translational Stroke Research*, 12:15–30, 2021.
- Rewa Sood and Mirabela Rusu. Anisotropic super resolution in prostate MRI using super resolution generative adversarial networks. In *2019 IEEE 16th International Symposium on Biomedical Imaging (ISBI 2019)*, pages 1688–1691, 2019.
- Jinglong Du, Zhongshi He, Lulu Wang, Ali Gholipour, Zexun Zhou, Dingding Chen, and Yuanyuan Jia. Super-resolution reconstruction of single anisotropic 3D MR images using residual convolutional neural network. *Neurocomputing*, 392:209–220, 2020.
- Kuan Zhang, Haoji Hu, Kenneth Philbrick, Gian Marco Conte, Joseph D Sobek, Pouria Rouzrokh, and Bradley J Erickson. SOUP-GAN: Super-resolution MRI using generative adversarial networks. *Tomography*, 8(2):905–919, 2022.
- Yuhua Chen, Anthony G Christodoulou, Zhengwei Zhou, Feng Shi, Yibin Xie, and Debiao Li. MRI super-resolution with GAN and 3D multi-level DenseNet: smaller, faster, and better, 2020. arXiv preprint arXiv:2003.01217.
- Qing Lyu, Hongming Shan, and Ge Wang. MRI super-resolution with ensemble learning and complementary priors. *IEEE Transactions on Computational Imaging*, 6:615–624, 2020.
- Andreas Lugmayr, Martin Danelljan, Luc Van Gool, and Radu Timofte. SRFlow: Learning the super-resolution space with normalizing flow. In *Computer Vision—ECCV 2020: 16th European Conference, Glasgow, UK, August 23–28, 2020, Proceedings, Part V 16*, pages 715–732. Springer, 2020.
- Youngeun Kim and Donghee Son. Noise conditional flow model for learning the super-resolution space. In *Proceedings of the IEEE/CVF Conference on Computer Vision and Pattern Recognition*, pages 424–432, 2021.
- Zhenhong Liu, Xingce Wang, Zhongke Wu, Yi-Cheng Zhu, and Alejandro F Frangi. Simultaneous Super-Resolution and Denoising on MRI via Conditional Stochastic Normalizing Flow. In *2023 IEEE International Conference on Bioinformatics and Biomedicine (BIBM)*, pages 1313–1318. IEEE, 2023.
- Kyungdeuk Ko, Bokyeung Lee, Jonghwan Hong, Donghyeon Kim, and Hanseok Ko. MRIFlow: Magnetic resonance image super-resolution based on normalizing flow and frequency prior. *Journal of Magnetic Resonance*, 352:107477, 2023.
- Zhanxiong Wu, Xuanheng Chen, Sangma Xie, Jian Shen, and Yu Zeng. Super-resolution of brain MRI images based on denoising diffusion probabilistic model. *Biomedical Signal Processing and Control*, 85:104901, 2023.
- Jueqi Wang, Jacob Levman, Walter Hugo Lopez Pinaya, Petru-Daniel Tudosiu, M Jorge Cardoso, and Razvan Marinescu. InverseSR: 3D Brain MRI Super-Resolution Using a Latent Diffusion Model. In *International Conference on Medical Image Computing and Computer-Assisted Intervention*, pages 438–447. Springer, 2023.
- Zejun Wu, Samuel W Remedios, Blake E Dewey, Aaron Carass, and Jerry L Prince. AniRes2D: anisotropic residual-enhanced diffusion for 2D MR super-resolution. In *Medical Imaging 2024: Clinical and Biomedical Imaging*, volume 12930, pages 567–574. SPIE, 2024a.
- Chih-Wei Chang, Junbo Peng, Mojtaba Safari, Elahheh Salari, Shaoyan Pan, Justin Roper, Richard LJ Qiu, Yuan Gao, Hui-Kuo Shu, Hui Mao, et al. High-resolution MRI synthesis using a data-driven framework with denoising diffusion probabilistic modeling. *Physics in Medicine & Biology*, 69(4):045001, 2024.
- Zhitao Han and Wenhui Huang. Arbitrary scale super-resolution diffusion model for brain MRI images. *Computers in Biology and Medicine*, 170:108003, 2024.
- Zhanxiong Wu, Xuanheng Chen, and Jiangnan Yu. 3D-SRDM: 3D super-resolution of MRI volumes based on diffusion model. *International Journal of Imaging Systems and Technology*, 34(3):e23093, 2024b.
- Zhisheng Lu, Juncheng Li, Hong Liu, Chaoyan Huang, Linlin Zhang, and Tiejong Zeng. Transformer for single image super-resolution. In *Proceedings of the IEEE/CVF conference on computer vision and pattern recognition*, pages 457–466, 2022.
- Fuzhi Yang, Huan Yang, Jianlong Fu, Hongtao Lu, and Baining Guo. Learning texture transformer network for image super-resolution. In *Proceedings of the IEEE/CVF conference on computer vision and pattern recognition*, pages 5791–5800, 2020.

- Chao Yan, Gen Shi, and Zhengliang Wu. Smir: A transformer-based model for mri super-resolution reconstruction. In *2021 IEEE International Conference on Medical Imaging Physics and Engineering (ICMIPE)*, pages 1–6. IEEE, 2021.
- Guangyuan Li, Jun Lv, Yapeng Tian, Qi Dou, Chengyan Wang, Chenliang Xu, and Jing Qin. Transformer-empowered multi-scale contextual matching and aggregation for multi-contrast MRI super-resolution. In *Proceedings of the IEEE/CVF conference on computer vision and pattern recognition*, pages 20636–20645, 2022.
- Chun-Mei Feng, Yunlu Yan, Huazhu Fu, Li Chen, and Yong Xu. Task transformer network for joint MRI reconstruction and super-resolution. In *Medical Image Computing and Computer Assisted Intervention–MICCAI 2021: 24th International Conference, Strasbourg, France, September 27–October 1, 2021, Proceedings, Part VI 24*, pages 307–317. Springer, 2021.
- Zhenting Zhou, Guoping Li, and Guozhong Wang. A hybrid of transformer and cnn for efficient single image super-resolution via multi-level distillation. *Displays*, 76:102352, 2023.
- Cristhian Forigua, Maria Escobar, and Pablo Arbelaez. Superformer: Volumetric transformer architectures for mri super-resolution. In *International Workshop on Simulation and Synthesis in Medical Imaging*, pages 132–141. Springer, 2022.
- Ming Cheng, Haoyu Ma, Qiufang Ma, Xiaopeng Sun, Weiqi Li, Zhenyu Zhang, Xuhan Sheng, Shijie Zhao, Junlin Li, and Li Zhang. Hybrid transformer and CNN attention network for stereo image super-resolution. In *Proceedings of the IEEE/CVF Conference on Computer Vision and Pattern Recognition*, pages 1702–1711, 2023.
- Jinsheng Fang, Hanjiang Lin, Xinyu Chen, and Kun Zeng. A hybrid network of CNN and transformer for lightweight image super-resolution. In *Proceedings of the IEEE/CVF conference on computer vision and pattern recognition*, pages 1103–1112, 2022.
- Yulun Zhang, Kunpeng Li, Kai Li, Lichen Wang, Bineng Zhong, and Yun Fu. Image super-resolution using very deep residual channel attention networks. In *Proceedings of the European conference on computer vision (ECCV)*, pages 286–301, 2018.
- Wenzhe Shi, Jose Caballero, Ferenc Huszár, Johannes Totz, Andrew P Aitken, Rob Bishop, Daniel Rueckert, and Zehan Wang. Real-time single image and video super-resolution using an efficient sub-pixel convolutional neural network. In *Proceedings of the IEEE conference on computer vision and pattern recognition*, pages 1874–1883, 2016.
- Amod Jog, Aaron Carass, and Jerry L Prince. Self super-resolution for magnetic resonance images. In *Medical Image Computing and Computer-Assisted Intervention–MICCAI 2016: 19th International Conference, Athens, Greece, October 17-21, 2016, Proceedings, Part III 19*, pages 553–560. Springer, 2016.
- Can Zhao, Aaron Carass, Blake E Dewey, Jonghye Woo, Jiwon Oh, Peter A Calabresi, Daniel S Reich, Pascal Sati, Dzung L Pham, and Jerry L Prince. A deep learning based anti-aliasing self super-resolution algorithm for MRI. In *Medical Image Computing and Computer Assisted Intervention–MICCAI 2018: 21st International Conference, Granada, Spain, September 16-20, 2018, Proceedings, Part I*, pages 100–108. Springer, 2018.
- Can Zhao, Muhan Shao, Aaron Carass, Hao Li, Blake E. Dewey, Lotta M. Ellingsen, Jonghye Woo, Michael A. Guttman, Ari M. Blitz, Maureen Stone, Peter A. Calabresi, Henry Halperin, and Jerry L. Prince. Applications of a deep learning method for anti-aliasing and super-resolution in MRI. *Magnetic Resonance Imaging*, 64:132–141, 2019. ISSN 0730-725X.
- Can Zhao, Blake E Dewey, Dzung L Pham, Peter A Calabresi, Daniel S Reich, and Jerry L Prince. SMORE: a self-supervised anti-aliasing and super-resolution algorithm for MRI using deep learning. *IEEE Transactions on Medical Imaging*, 40(3):805–817, 2020.
- Samuel W Remedios, Shuo Han, Blake E Dewey, Dzung L Pham, Jerry L Prince, and Aaron Carass. Joint image and label self-super-resolution. In *Simulation and Synthesis in Medical Imaging: 6th International Workshop, SASHIMI 2021, Held in Conjunction with MICCAI 2021, Strasbourg, France, September 27, 2021, Proceedings 6*, pages 14–23. Springer, 2021.
- Samuel W Remedios, Shuo Han, Lianrui Zuo, Aaron Carass, Dzung L Pham, Jerry L Prince, and Blake E Dewey. Self-supervised super-resolution for anisotropic MR images with and without slice gap. In *International Workshop on Simulation and Synthesis in Medical Imaging*, pages 118–128. Springer, 2023.
- Shuo Han, Samuel Remedios, Aaron Carass, Michael Schär, and Jerry L Prince. MR slice profile estimation by learning to match internal patch distributions. In *International Conference on Information Processing in Medical Imaging*, page 108–119, Berlin, Heidelberg, 2021. Springer-Verlag.
- Shuo Han, Samuel W. Remedios, Michael Schär, Aaron Carass, and Jerry L. Prince. ESPRESO: An algorithm to estimate the slice profile of a single magnetic resonance image. *Magnetic Resonance Imaging*, 98:155–163, 2023. ISSN 0730-725X.

- Jiahui Yu, Yuchen Fan, Jianchao Yang, Ning Xu, Xinchao Wang, and Thomas S Huang. Wide activation for efficient and accurate image super-resolution, 2018. arXiv preprint arXiv:1808.08718.
- Radu Timofte, Vincent De Smet, and Luc Van Gool. Anchored neighborhood regression for fast example-based super-resolution. In *Proceedings of the IEEE international conference on computer vision*, pages 1920–1927, 2013.
- Mauricio Delbracio and Guillermo Sapiro. Removing camera shake via weighted fourier burst accumulation. *IEEE Transactions on Image Processing*, 24(11):3293–3307, 2015.
- Bee Lim, Sanghyun Son, Heewon Kim, Seungjun Nah, and Kyoung Mu Lee. Enhanced deep residual networks for single image super-resolution. In *Proceedings of the IEEE conference on computer vision and pattern recognition workshops*, pages 136–144, 2017.
- Jeong Joon Park, Peter Florence, Julian Straub, Richard Newcombe, and Steven Lovegrove. DeepSDF: Learning continuous signed distance functions for shape representation. In *Proceedings of the IEEE/CVF Conference on Computer Vision and Pattern Recognition*, pages 165–174, 2019.
- Ben Mildenhall, Pratul P. Srinivasan, Matthew Tancik, Jonathan T. Barron, Ravi Ramamoorthi, and Ren Ng. NeRF: Representing Scenes as Neural Radiance Fields for View Synthesis. In *ECCV*, pages 405–421, Cham, 2020. Springer International Publishing.
- Vincent Sitzmann, Julien Martel, Alexander Bergman, David Lindell, and Gordon Wetzstein. Implicit neural representations with periodic activation functions. *Advances in Neural Information Processing Systems*, 33:7462–7473, 2020.
- Yinbo Chen, Sifei Liu, and Xiaolong Wang. Learning continuous image representation with local implicit image function. In *Proceedings of the IEEE/CVF Conference on Computer Vision and Pattern Recognition*, pages 8628–8638, 2021.
- Qing Wu, Yuwei Li, Yawen Sun, Yan Zhou, Hongjiang Wei, Jingyi Yu, and Yuyao Zhang. An arbitrary scale super-resolution approach for 3D MR images via implicit neural representation. *IEEE Journal of Biomedical and Health Informatics*, 27(2):1004–1015, 2022.
- Chuan Tan, Jin Zhu, and Pietro Lio'. Arbitrary scale super-resolution for brain MRI images. In *IFIP International Conference on Artificial Intelligence Applications and Innovations*, pages 165–176. Springer, 2020.
- Jin Zhu, Chuan Tan, Junwei Yang, Guang Yang, and Pietro Lio'. Arbitrary scale super-resolution for medical images. *International Journal of Neural Systems*, 31(10):2150037, 2021.
- Hongying Liu, Zekun Li, Fanhua Shang, Yuanyuan Liu, Liang Wan, Wei Feng, and Radu Timofte. Arbitrary-scale super-resolution via deep learning: A comprehensive survey. *Information Fusion*, 102:102015, 2024.
- Julian McGinnis, Suprosanna Shit, Hongwei Bran Li, Vasiliki Sideri-Lampretsa, Robert Graf, Maik Dannecker, Jiazhen Pan, Nil Stolt-Ansó, Mark Mühlau, Jan S Kirschke, et al. Single-subject Multi-contrast MRI Super-resolution via Implicit Neural Representations. In *International Conference on Medical Image Computing and Computer-Assisted Intervention*, pages 173–183. Springer, 2023.
- Juan E Iglesias, Benjamin Billot, Yaël Balbastre, Colin Magdamo, Steven E Arnold, Sudeshna Das, Brian L Edlow, Daniel C Alexander, Polina Golland, and Bruce Fischl. SynthSR: A public AI tool to turn heterogeneous clinical brain scans into high-resolution T1-weighted images for 3D morphometry. *Science advances*, 9(5):eadd3607, 2023.
- John Pauly, Patrick Le Roux, Dwight Nishimura, and Albert Macovski. Parameter relations for the Shinnar-Le Roux selective excitation pulse design algorithm (NMR imaging). *IEEE transactions on medical imaging*, 10(1):53–65, 1991.
- Meir Shinnar, Scott Eleff, Harihara Subramanian, and John S Leigh. The synthesis of pulse sequences yielding arbitrary magnetization vectors. *Magnetic resonance in medicine*, 12(1):74–80, 1989.
- Pauli Virtanen, Ralf Gommers, Travis E. Oliphant, Matt Haberland, Tyler Reddy, David Cournapeau, Evgeni Burovski, Pearu Peterson, Warren Weckesser, Jonathan Bright, Stéfan J. van der Walt, Matthew Brett, Joshua Wilson, K. Jarrod Millman, Nikolay Mayorov, Andrew R. J. Nelson, Eric Jones, Robert Kern, Eric Larson, C J Carey, İlhan Polat, Yu Feng, Eric W. Moore, Jake VanderPlas, Denis Laxalde, Josef Perktold, Robert Cimrman, Ian Henriksen, E. A. Quintero, Charles R. Harris, Anne M. Archibald, Antônio H. Ribeiro, Fabian Pedregosa, Paul van Mulbregt, and SciPy 1.0 Contributors. SciPy 1.0: Fundamental Algorithms for Scientific Computing in Python. *Nature Methods*, 17:261–272, 2020.
- Adam Paszke, Sam Gross, Francisco Massa, Adam Lerer, James Bradbury, Gregory Chanan, Trevor Killeen, Zeming Lin, Natalia Gimelshein, Luca Antiga, et al. Pytorch: An imperative style, high-performance deep learning library. *Advances in neural information processing systems*, 32, 2019.
- Shuo Han. *Cerebellum parcellation from magnetic resonance imaging using deep learning*. PhD thesis, Johns Hopkins University, Baltimore, MD, March 2022.

- Diederik P Kingma and Jimmy Ba. Adam: A method for stochastic optimization, 2014. arXiv preprint arXiv:1412.6980.
- Leslie N Smith and Nicholay Topin. Super-convergence: Very fast training of neural networks using large learning rates. In *Artificial intelligence and machine learning for multi-domain operations applications*, volume 11006, pages 369–386. SPIE, 2019.
- J Martin, Frank Ong, Jun Ma, Jonathan I Tamir, Michael Lustig, and William A Grissom. SigPy. RF: Comprehensive open-source RF pulse design tools for reproducible research, 2020. Proceedings of the International Society for Magnetic Resonance in Medicine. ISMRM Annual Meeting.
- Pamela J. LaMontagne, Tammie LS. Benzinger, John C. Morris, Sarah Keefe, Russ Hornbeck, Chengjie Xiong, Elizabeth Grant, Jason Hassenstab, Krista Moulder, Andrei G. Vlassenko, Marcus E. Raichle, Carlos Cruchaga, and Daniel Marcus. OASIS-3: Longitudinal neuroimaging, clinical, and cognitive dataset for normal aging and Alzheimer disease, 2019. medRxiv.
- Žiga Lesjak, Alfiia Galimzianova, Aleš Koren, Matej Lukin, Franjo Pernuš, Boštjan Likar, and Žiga Špiclin. A novel public MR image dataset of multiple sclerosis patients with lesion segmentations based on multi-rater consensus. *Neuroinformatics*, 16:51–63, 2018.
- Mengye Lyu, Lifeng Mei, Shoujin Huang, Sixing Liu, Yi Li, Kexin Yang, Yilong Liu, Yu Dong, Linzheng Dong, and Ed X Wu. M4Raw: A multi-contrast, multi-repetition, multi-channel MRI k-space dataset for low-field MRI research. *Scientific Data*, 10(1):264, 2023.
- Lin Guo, Samuel W Remedios, Alexandru Korotcov, and Dzung L Pham. Self-supervised super-resolution of 2-D pre-clinical MRI acquisitions. In *Medical Imaging 2024: Clinical and Biomedical Imaging*, volume 12930, pages 652–658. SPIE, 2024.
- Stefan Van der Walt, Johannes L Schönberger, Juan Nunez-Iglesias, François Boulogne, Joshua D Warner, Neil Yager, Emmanuelle Gouillart, and Tony Yu. scikit-image: image processing in python. *PeerJ*, 2:e453, 2014.
- Yuankai Huo, Zhoubing Xu, Yunxi Xiong, Katherine Aboud, Prasanna Parvathaneni, Shunxing Bao, Camilo Bermudez, Susan M Resnick, Laurie E Cutting, and Bennett A Landman. 3D whole brain segmentation using spatially localized atlas network tiles. *NeuroImage*, 194:105–119, 2019.
- Benjamin Billot, Douglas N Greve, Oula Puonti, Axel Thielscher, Koen Van Leemput, Bruce Fischl, Adrian V Dalca, Juan Eugenio Iglesias, et al. SynthSeg: Segmentation of brain MRI scans of any contrast and resolution without retraining. *Medical image analysis*, 86:102789, 2023.
- Jinwei Zhang, Lianrui Zuo, Blake E Dewey, Samuel W Remedios, Savannah P Hays, Dzung L Pham, Jerry L Prince, and Aaron Carass. Harmonization-enriched domain adaptation with light fine-tuning for multiple sclerosis lesion segmentation. In *Medical Imaging 2024: Clinical and Biomedical Imaging*, volume 12930, pages 635–641. SPIE, 2024.
- Yochai Blau and Tomer Michaeli. The perception-distortion tradeoff. In *Proceedings of the IEEE conference on computer vision and pattern recognition*, pages 6228–6237, 2018.